

# Learning to Generalize towards Unseen Domains via a Content-Aware Style Invariant Model for Disease Detection from Chest X-rays

Mohammad Zunaed, *Student Member, IEEE*, Md. Aynal Haque, *Senior Member, IEEE*, and Taufiq Hasan, *Senior Member, IEEE*

**Abstract**—Performance degradation due to source domain mismatch is a longstanding challenge in deep learning-based medical image analysis, particularly for chest X-rays (CXRs). Several methods (e.g., adversarial training, multi-domain mix-ups) have been proposed to extract domain-invariant high-level features to address this domain shift. However, these methods do not explicitly regularize the content and style characteristics of the extracted domain-invariant features. Recent studies have demonstrated that CNN models exhibit a strong bias toward styles (e.g., uninformative textures) rather than content (e.g., shape), in stark contrast to the human-vision system. Radiologists tend to learn visual cues from CXRs and thus perform well across multiple domains. Therefore, in medical imaging for pathology diagnosis from CXR images, models should extract domain-invariant features that are style-invariant and content-biased. Motivated by this, we employ the novel style randomization modules (SRMs) at both image and feature levels that work together hierarchically to create rich style perturbed features on the fly while keeping the content intact. In addition, we leverage consistency regularizations between global semantic features and predicted probability distributions, respectively, for with and without style perturbed versions of the same CXR image to tweak the model’s sensitivity toward content markers for accurate predictions. Extensive experiments with three large-scale thoracic disease datasets, i.e., CheXpert, MIMIC-CXR, and BRAX, demonstrate that our proposed framework is more robust in the presence of domain shift and achieves state-of-the-art performance.

**Index Terms**—Chest X-ray, domain generalization, neural style transfer, thoracic disease classification.

## I. INTRODUCTION

DEEP learning algorithms have demonstrated remarkable performance in pathology detection from chest X-ray (CXR) images in recent years [1]–[5]. However, despite the promising performance of current deep learning architectures, one major bottleneck is the performance drop on unseen domain data compared to internal data due to distribution discrepancy, also known as domain shift [6]. This phenomenon

hinders the practical applicability of deep learning models for medical image analyses in real-world scenarios. A number of approaches, i.e., domain adaptation (DA) [7]–[11] and domain generalization (DG) [12]–[15] methods, have been developed over time to address this domain shift.

Recent studies have demonstrated that convolutional neural networks (CNNs) exhibit a strong bias toward style rather than content for classification [16], [17]. Geirhos *et al.* [17] showed that CNNs are vulnerable to any changes in image statistics from those on which they are trained. As a result, the CNNs are intrinsically more susceptible to domain shift compared to the human visual system. However, Geirhos *et al.* [17] demonstrated that the heavy texture bias nature of the CNNs can be overcome and tuned toward content bias by utilizing a suitable dataset for training. Jackson *et al.* [18] showed that data augmentation via style transfer with artistic paintings could improve the model’s robustness to domain shift for computer vision tasks for natural images. Several DG methods for natural images [19]–[22] have recently been developed to leverage neural style manipulation for improving cross-domain performances.

Motivated by the impact of neural style randomization on DG for natural images, we experiment with the style statistics of CXR images at both the image and feature levels. First, we plot the mean and standard deviation of CXR images (i.e., image-level style features) from three large-scale thoracic diseases datasets, i.e., CheXpert [23], MIMIC-CXR [24], and BRAX [25]. We also plot the 2D t-SNE [26] visualization of feature-level style statistics (i.e., concatenation of means and standard deviations [27]) computed from the first dense block of DenseNet-121 [28] trained on the three thoracic disease datasets. The plots are illustrated in Fig. 1. We can observe from Fig. 1 that a domain distribution gap based on style statistics exists among these datasets at the image level. The t-SNE plot of the feature statistics from the first dense block demonstrates that the model captures this uninformative domain information of styles specific to each thoracic disease dataset, which is reflected by the separable clusters. A robust machine-learning model should not be susceptible to these global image statistics. In real-world scenarios, radiologists tend to learn visual cues from CXRs, rather than uninformative textures and thus perform well across multiple domains. Therefore, in medical imaging for pathology diagnosis from CXR images, robust machine-learning models should not rely on these global image statistics. Instead, they should extract

Mohammad Zunaed is with the Department of Electrical and Electronic Engineering and also with the mHealth Lab, Department of Biomedical Engineering, Bangladesh University of Engineering and Technology, Dhaka-1205, Bangladesh. (e-mail: rafizunaed@gmail.com)

Md. Aynal Haque is with the Department of Electrical and Electronic Engineering, Bangladesh University of Engineering and Technology, Dhaka-1205, Bangladesh. (e-mail: aynal@eee.buet.ac.bd)

Taufiq Hasan is with the mHealth Lab, Department of Biomedical Engineering, Bangladesh University of Engineering and Technology, Dhaka-1205, Bangladesh, and the Center for Bioengineering Innovation and Design (CBID), Department of Biomedical Engineering, Johns Hopkins University, Baltimore, MD. (e-mail: taufiq@bme.buet.ac.bd and taufiq.hasan@jhu.edu)

domain-invariant features that are style-invariant and content-biased (pathology traits).

However, to the best of our knowledge, no previous study has utilized the application of neural style randomization for domain-agnostic thoracic disease detection from CXR images. DG approaches for natural images based on style randomization [19], [29], [30] diversify the training data by synthesizing new styles from the existing sources available during training to simulate unseen domain data. As a result, these methods' augmentation range is sensitive and limited to the style diversity range of the source datasets, which may result in suboptimal performance. In addition, they utilized pre-defined parameters, i.e., mean and standard deviation, as the style embeddings [19], [22], [29]. Learnable pixel-wise style embeddings may improve the performance further. Moreover, consistency regularizations between global semantic features and probability distributions of different augmented versions of the same CXR image are not well studied.

In this work, we propose a novel domain-agnostic, content-biased, and style-invariant DG framework that can be trained in single or multi-source domain settings without explicit domain labels. We employ style randomization modules (SRMs) at the image and feature levels to hierarchically augment the style while preserving the pathology-specific content traits. Utilizing the prior maximum and minimum pixel value knowledge of a normalized CXR image, we construct a set for sampling mean and standard deviation to use them for switching style characteristics at the image level. For feature-level style augmentation, we deploy a learnable SRM module that generates the pixel-wise style embeddings instead of setting pre-defined parameters, i.e., channel-wise mean and standard deviations as affine parameter values [27], for style manipulation. In addition, we employ two consistency regularization losses to enforce the consistency of semantic global feature maps and the predicted probability distributions, respectively, between the original CXR and the style-perturbed CXR. The variability of styles between different perturbations of the same CXR with content information intact makes the style attribute unreliable and makes the model focus more on pathology-specific content in making a decision. The contributions of this paper are summarized as follows:

- We employ a novel SRM at the image level that uses the prior knowledge of possible maximum and minimum pixel values of a CXR to create a set to randomly sample and swap style characteristics.
- We propose a novel feature-level SRM module that learns the pixel-level affine parameters instead of utilizing pre-defined style embeddings for creating more rich, diversified style-perturbed features on the fly.
- We enforce the consistency regularization losses between the global semantic feature maps and the probability distributions for CXRs with and without style characteristics perturbed to guide the model toward content-related cues.
- We perform extensive experiments with three large-scale datasets, i.e., CheXpert [23], MIMIC-CXR [24], and Brax [25]. Our proposed framework demonstrates consistent improvements and outperforms competing approaches under different cross-domain settings.

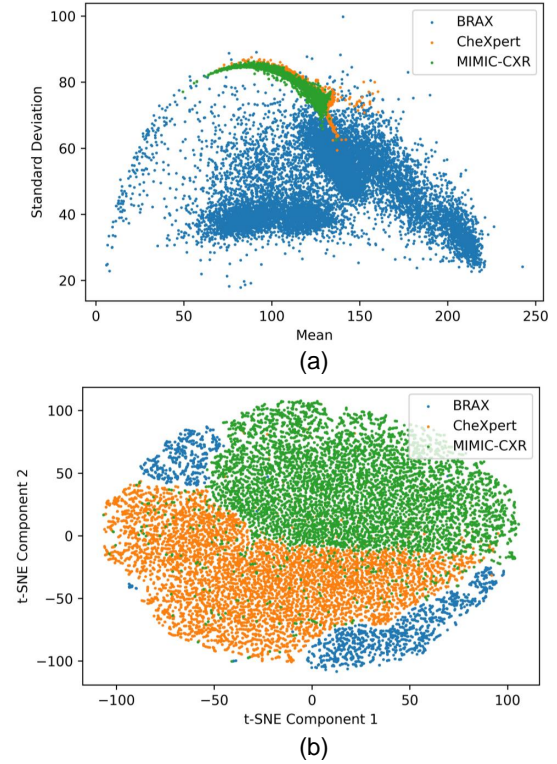


Fig. 1. (a) Illustration of image-level distribution gap of three thoracic disease datasets using image-level style embeddings, i.e., mean and standard deviation. (b) 2D t-SNE visualization of style statistics (concatenation of means and standard deviations) computed from the feature maps from the first dense block of the DenseNet-121, trained on the thoracic datasets. We can observe that the feature statistics capture dataset-specific styles reflected by the separable clusters.

## II. RELATED WORK

**Domain Adaptation (DA):** Most past DA approaches have been developed to minimize measures of distances between the source domain and the target domain features [31]. Recent methods for DA can be categorized into adversarial training-based domain alignment [7], [8], [11], [32], [33], Fourier transform-based methods [34], generative adversarial networks (GANs) based methods (unpaired image-to-image translation into source/target domain) [35]–[37], high-level feature map alignment based on similarity measurement [8], [9], gradient reversal based alignment methods [38], and others.

Luo *et al.* [7] adopted class-wise adversarial training to alleviate feature differences across common categories of two datasets to mine the knowledge from the external thoracic disease dataset to improve the performance of the classifier on the internal thoracic disease dataset. Pham *et al.* [32] fed the predicted class information to the discriminator to condition the discriminator to avoid any conflict between the generalized latent feature representation with a feature representation that is suitable for the actual classification task. Zhang *et al.* [8] proposed a domain, instance, and perturbation invariance learning-based framework for utilizing unsupervised domain adaptive thorax disease classification. Diao *et al.* [37] proposed a histogram-based GAN methodology for DA that captured the variations in global intensity changes by transforming

histograms along with individual pixel intensities. Yang *et al.* [34] employed the Fourier transform to alleviate the domain discrepancy. They swapped the low-frequency amplitude components between the source and target images while keeping the phase components unaltered to diversify the training dataset. Afterward, they used the modified amplitude and unaltered phase components to reconstitute the altered images and then utilized them to train the deep learning model.

However, a significant limitation of the DA methods is that they require explicit domain labels, i.e., source and target domains or multiple domains, which is often unavailable in most real-world medical applications due to annotation cost or privacy reasons. In addition, most real-world medical datasets usually consist of data from multiple medical sites using various scanners, i.e., ambiguous domain labels. Moreover, they require re-training during application on new target domains, which is inconvenient and impractical for deploying models in real-world medical image analysis applications.

**Domain Generalization (DG):** DG approaches aim to utilize the source domains only during training and generalize toward any unseen target domain without requiring prior access or re-training. DG is considered more challenging than DA approaches, as the target domain samples are not exposed during the training phase. DG methods can be categorized into three broad approaches, i.e., augmentation-based methods [12]–[14], alignment-based methods [39], [40], and meta-learning-based methods [15]. DG methods can be further divided based on the number of source domains utilized during training: multi-source DG and single-source DG. Multi-source DG assumes multiple relevant domains are available during training. Utilizing multiple source domains allows a deep learning model to discover stable patterns across source domains to better generalize to unseen domains. In contrast, the single-source DG is trained with only one source domain and is expected to generalize toward unseen domains.

Wang *et al.* [12] performed the mixup operation of CXRs from multiple domains to create a virtual domain and utilized ensemble learning to improve performance in unseen domains. However, this approach requires at least two available domains to perform the mixup. Zhang *et al.* [13] exploited a series of extensive deep-stacked augmentations during training to simulate the expected domain shift to address DG on unseen data. However, data augmentation-based methods often require carefully selecting augmentation methods to resemble the unseen domain's appearance.

Recent literature studies have shown that CNNs demonstrate a strong bias toward style rather than content and are sensitive to any shift from image statistics that they are trained on, limiting their DG capability [16], [17]. Motivated by the impact of neural style transfer on the domain shift, a number of DG methods have been proposed based on neural style randomization. DG methods based on style randomization can be divided into two categories, i.e., feature-level and image-level randomizations.

The feature-level randomization includes the perturbation of feature statistics from intermediate convolutional layers of the backbone model. Nuriel *et al.* [29] applied adaptive instance normalization to swap the style statistics between

activations of permuted and non-permuted samples in a mini-batch to reduce the representation of global statistics in the classifier model. Zhou *et al.* [19] proposed a novel parameter-free module MixStyle that synthesizes new domains by probabilistically mixing feature statistics between instances. Nam *et al.* [21] utilized adaptive instance normalization along with adversarial learning to reduce the intrinsic style bias. Tang *et al.* [30] proposed two novel modules named CrossNorm and SelfNorm for swapping feature statistics and recalibrating the statistics through attention to both diversify and bridge the gap between source and target domains. Wang *et al.* [22] developed an encoder-decoder-like architecture named FSR to integrate random noise with the original style parameters to generate new style embeddings. However, these methods use the pre-defined parameters, i.e., channel-wise mean and standard deviation, as the style embeddings. Instead of pre-defined parameters, pixel-wise learnable style parameters may yield more diverse and hard style statistics, resulting in a more robust DG model.

The image-level style randomization-based methods try to diversify the training dataset by constructing hard stylized samples. Zhong *et al.* [20] proposed a novel augmentation approach, named adversarial style augmentation (AdvStyle), to generate diverse stylized images by adversarially learning the image-level style features to reduce overfitting on the source domain and be robust towards style variations of unknown domains. Yamashita *et al.* [14] introduced a form of data augmentation named STRAP, based on random style transfer with medically irrelevant style sources for improving DG performance. However, this approach requires training an additional model to perform the stylization. Moreover, the stylized dataset is prepared before the training, limiting the on-the-fly opportunity of creating diverse augmentations.

Previous image-level and feature-level style randomization-based DG approaches synthesize style or swap style statistics based on the source domains available during training. Thus, the diversity of the augmented samples is limited and sensitive to the available source domains. Furthermore, the exploitation of semantic content consistency between the original and perturbed activation feature maps will allow for robust feature learning and maximize the effectiveness of style augmentation for the out-of-distribution performance of the model.

Overall, to the best of our knowledge, the application of neural style randomization for deriving a DG model for thoracic disease detection from CXRs is not well studied. A systematic exploration of the potential of extracting content-specific (pathology-dependent) but style-invariant domain-agnostic features may further improve DG performance.

### III. METHODOLOGY

#### A. Preliminaries

1) *Instance Normalization:* Ulyanov *et al.* [41] proposed instance normalization (IN) for better stylization performance. Let the activation feature map,  $\mathbf{X}_1 \in \mathbb{R}^{D \times W \times H}$ , where,  $H$

and  $W$  indicate spatial dimensions, and  $D$  is the number of channels. IN of feature matrix  $\mathbf{X}_1$  is formulated as,

$$\mu(X_1)_i = \frac{1}{WH} \sum_{j=1}^W \sum_{k=1}^H (X_1)_{i,j,k} \quad (1)$$

$$\sigma(X_1)_i = \sqrt{\frac{1}{WH} \sum_{j=1}^W \sum_{k=1}^H [(X_1)_{i,j,k} - \mu(X_1)_i]^2 + \epsilon} \quad (2)$$

$$\text{IN}(\mathbf{X}_1) = \gamma \left( \frac{\mathbf{X}_1 - \mu(\mathbf{X}_1)}{\sigma(\mathbf{X}_1)} \right) + \beta \quad (3)$$

Here,  $i \in \{1, 2, \dots, D\}$ ,  $\gamma, \beta \in \mathbb{R}^D$  are learnable affine vectors, and  $\epsilon$  is a very small constant for stability.

2) *Adaptive Instance Normalization*: Huang *et al.* [27] proposed a parameter-less module named adaptive instance normalization (AdaIN) that can change the style of a convolutional feature activation map to any given arbitrary style utilizing the convolutional feature's channel-wise mean and standard deviation as the style statistics. For example, if we want to convert the style of feature map  $\mathbf{X}_1$  to that of  $\mathbf{X}_2 \in \mathbb{R}^{D \times W \times H}$ , the channel-wise mean and standard deviation of  $\mathbf{X}_2$  will be computed and be used as affine parameters in instance normalization for stylization.

$$\mu(X_2)_i = \frac{1}{WH} \sum_{j=1}^W \sum_{k=1}^H (X_2)_{i,j,k} \quad (4)$$

$$\sigma(X_2)_i = \sqrt{\frac{1}{WH} \sum_{j=1}^W \sum_{k=1}^H [(X_2)_{i,j,k} - \mu(X_2)_i]^2 + \epsilon} \quad (5)$$

$$\text{AdaIN}(\mathbf{X}_1, \mathbf{X}_2) = \sigma(\mathbf{X}_2) \left( \frac{\mathbf{X}_1 - \mu(\mathbf{X}_1)}{\sigma(\mathbf{X}_1)} \right) + \mu(\mathbf{X}_2) \quad (6)$$

In this paper, we will leverage the AdaIN to perturb the style statistics at the image level. For feature-level style perturbation, we will learn the affine parameters for each pixel level for any arbitrary styles instead of using pre-defined channel-wise mean and standard deviation parameters.

3) *Kullback-Leibler Divergence loss*: The Kullback-Leibler divergence (KLD) loss is generally applied to minimize the difference between two probability distributions. For example, if we try to reduce the distribution gap between probability distributions,  $\mathbf{y}_{\text{pred}}$  and  $\mathbf{y}_{\text{true}}$ , the loss is defined as:

$$\text{KLD}(\mathbf{y}_{\text{pred}}, \mathbf{y}_{\text{true}}) = \mathbf{y}_{\text{true}} \log \frac{\mathbf{y}_{\text{true}}}{\mathbf{y}_{\text{pred}}} \quad (7)$$

Where  $\mathbf{y}_{\text{true}}$  is the target distribution and  $\mathbf{y}_{\text{pred}}$  is generally the output from a model. In our proposed method, we will derive two probability distributions,  $\mathbf{y}_1$ , and  $\mathbf{y}_2$ , one for images with style perturbed and the other without style perturbed. As there are no ground truth probability distributions, to minimize the discrepancy between these predicted probability distributions, we define the KLD loss as:

$$\text{KLD}'(\mathbf{y}_1, \mathbf{y}_2) = \frac{\mathbf{y}_1^* \log \frac{\mathbf{y}_1^*}{\mathbf{y}_2} + \mathbf{y}_2^* \log \frac{\mathbf{y}_2^*}{\mathbf{y}_1}}{2} \quad (8)$$

Note that \* indicates that the gradient is not propagated through that parameter, as suggested by Miyato *et al.* [42], to avoid the model collapse issue.

## B. Image-Level Style Perturbation (SRM-IL)

Let the possible maximum and minimum value of a pixel of a normalized CXR image is  $x_{\max}$  and  $x_{\min}$ , respectively. Regardless of any domain invariance, the style parameter, such as channel-wise mean and standard deviation, will be limited to this range. For any CXR image  $\mathbf{I} \in \mathbb{R}^{w \times h}$ , we randomly sample  $\mu(\mathcal{S})$  and  $\sigma(\mathcal{S})$  from the set of values  $\mathcal{S} = [x_{\min}, x_{\max}]$  and use them to transfer the style of the CXR image. Here,  $h$  and  $w$  indicate spatial dimensions. For typical normalized CXR images, the values range from 0 to 255. For other modalities, the maximum and minimum values can be set accordingly.

$$\text{SRM-IL}(\mathbf{I}, \mu(\mathcal{S}), \sigma(\mathcal{S})) = \mathbf{I}_s = \sigma(\mathcal{S}) \left( \frac{\mathbf{I} - \mu(\mathbf{I})}{\sigma(\mathbf{I})} \right) + \mu(\mathcal{S}) \quad (9)$$

Contrary to the previous methods, we do not utilize existing samples from the source domains for style randomization. As a result, our style diversity is not limited to source domains and can create a more diverse set of global statistics.

## C. Feature-Level Style Perturbation (SRM-FL)

In medical image segmentation, it has been demonstrated that multiple stacked augmentations or strong augmentations can effectively improve a model's robustness to domain shift [13]. Inspired by this finding, we apply the style perturbation not only at the image level but also at the feature level. The feature-level style randomization module takes content ( $\mathbf{X}_c \in \mathbb{R}^{D \times W \times H}$ ) and reference style ( $\mathbf{X}_{rs} \in \mathbb{R}^{D \times W \times H}$ ) activation maps and transfers the style of the content activation maps to that of the style activation maps. We deploy two style learning nets, i.e., GammaNet ( $\phi_\gamma$ ) and BetaNet ( $\phi_\beta$ ), to learn the pixel-level affine transformation parameters for transferring style to the content activation maps. The GammaNet and BetaNet shares similar architecture, comprised of four convolutional layers. The initial and the last convolutional layers contain kernels of  $1 \times 1$  with the same number of channels as the input feature map. The second and third convolutional layers have filters with  $3 \times 3$  dimensions, with channel dimensions following the squeeze and excitation block structure [43], i.e., the second block reduces the channel number, while the third block expands the channel number. The style nets do not contain any non-linear activation functions or normalization layers. The output from these two nets,  $\phi_\gamma(\mathbf{X}_{rs}) \in \mathbb{R}^{D \times W \times H}$ , and  $\phi_\beta(\mathbf{X}_{rs}) \in \mathbb{R}^{D \times W \times H}$ , are set as the affine transformation parameters in the instance normalization to transfer the style statistics.

$$\begin{aligned} \text{SRM-FL}(\mathbf{X}_c, \mathbf{X}_{rs}) &= \mathbf{X}_s \\ &= \phi_\gamma(\mathbf{X}_{rs}) \left( \frac{\mathbf{X}_c - \mu(\mathbf{X}_c)}{\sigma(\mathbf{X}_c)} \right) + \phi_\beta(\mathbf{X}_{rs}) \end{aligned} \quad (10)$$

To train the style nets, we utilize the content and style loss. The content and style loss are defined as:

$$\mathcal{L}_c = \|\mathbf{X}_c - \mathbf{X}_s\|_F^2 \quad (11)$$

$$\mathcal{L}_s = \|\mathcal{G}(\mathbf{X}_{rs}) - \mathcal{G}(\mathbf{X}_s)\|_F^2 \quad (12)$$

$$\mathcal{L}_\phi = \mathcal{L}_c + \eta \mathcal{L}_s \quad (13)$$

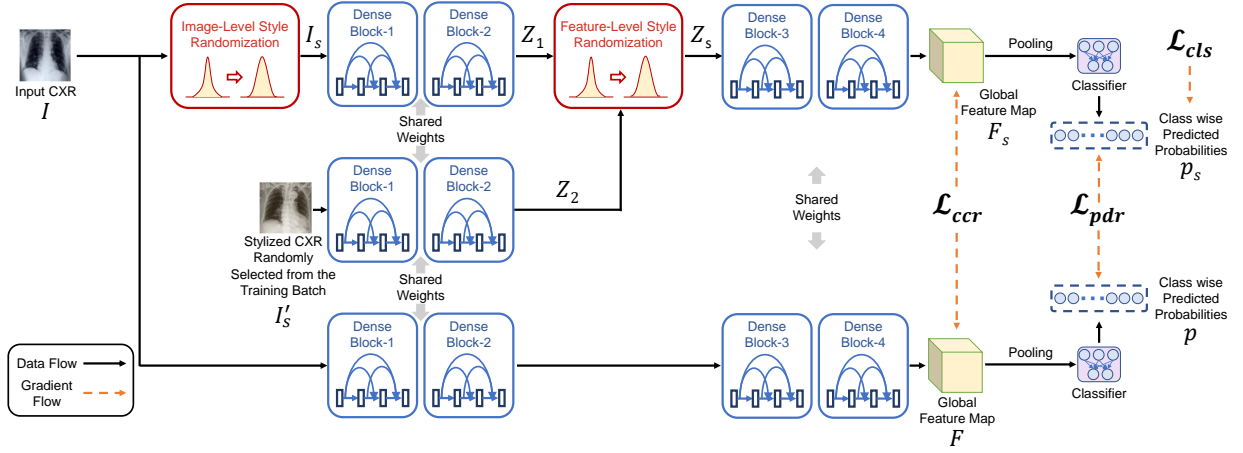


Fig. 2. Overview of the proposed framework. The style statistics of the input CXR are randomized with the randomly sampled mean and standard deviation from the set of values constructed from the prior knowledge of possible maximum and minimum values. Both CXRs, with or without style randomized, are passed to the shared feature extractor, DenseIBN-121, to generate two global feature spaces. For the stylized CXR, another round of style randomization is applied to the feature space after dense block-2, with a feature space for a randomly selected stylized CXR from the training mini-batch. The content consistency loss is employed between the two global feature spaces to increase the model's bias toward disease-specific content. In addition, a Kullback-Leibler divergence-based regularization loss is applied between the predicted probability distributions for CXRs with and without style statistics perturbed. The global feature space from the stylized CXR is pooled and passed to the classifier for pathology prediction.

Here,  $\|\cdot\|_F$  denotes the Frobenius norm, and  $\mathcal{G}(\cdot)$  represents the Gram matrix. The  $\eta$  is a hyperparameter.

#### D. Domain Agnostic Network

The overall proposed framework is illustrated in Fig. 2. We adopt DenseIBN-121 [44], pre-trained on the ImageNet dataset [45], as the backbone of our framework. Furthermore, we replace the last fully connected (FC) layer with an FC layer with  $N$  output neurons, where  $N$  denotes the class number.

We take a CXR image  $I$  and apply image-level style perturbation to get perturbed CXR image  $I_s$ . The pathology traits or content information remain the same in both images. The stylized CXR image  $I_s$  is passed through the dense block-1,2 to generate the intermediate feature space  $Z_1 \in \mathbb{R}^{D \times W \times H}$ . Let  $Z_2 \in \mathbb{R}^{D \times W \times H}$  be the intermediate feature matrix after the dense block-1,2 for a randomly sampled stylized CXR image  $I_s'$  from the training mini-batch. We apply the SRM-FL on  $Z_1$  and  $Z_2$  to switch the feature statistics of  $Z_1$  with that of  $Z_2$ .

$$Z_s = \text{SRM-FL}(Z_1, Z_2) \quad (14)$$

Here, SRM-FL( $\cdot$ ) denotes the feature level style randomization module. Afterward, the feature space  $Z_s \in \mathbb{R}^{D \times W \times H}$  is passed to the dense block-3,4 to generate the global feature map  $F_s \in \mathbb{R}^{D' \times W' \times H'}$ . Here,  $D'$ ,  $H'$ , and  $W'$  denote the feature map depth, height, and width, respectively.

**Classification Loss:** The feature space  $F_s$  is pooled and fed to the classifier network, which consists of one FC layer and one sigmoid layer. Let the predicted probability vector  $p^s \in \mathbb{R}^N$ .  $N$  is the total number of pathologies. The pathological ground truths are expressed as a  $N$ -dimensional label vector,  $L = [l_1, \dots, l_i, \dots, l_N]$  where  $l_i \in \{0, 1\}$ ,  $N = 14$ . Here,  $l_i$  represents whether there is any pathology, i.e., 1 for presence

and 0 for absence. Following [46], we utilize the focal loss [47] as the classification loss due to class imbalance:

$$\mathcal{L}_{cls} = -\alpha_i^t (1 - p_i^t)^{\gamma'} \log(p_i^t) \quad (15)$$

$$p_i^t = \begin{cases} p_i^s & \text{if } l_i = 1 \\ 1 - p_i^s & \text{otherwise} \end{cases} \quad (16)$$

$$\alpha_i^t = \begin{cases} \alpha^t & \text{if } l_i = 1 \\ 1 - \alpha_i^t & \text{otherwise} \end{cases} \quad (17)$$

Here,  $i \in \{1, 2, \dots, N\}$ . The  $\alpha^t$  and  $\gamma'$  are the balancing and focusing hyper-parameter from the original paper [47].

**Consistency Regularization Loss:** The CXR without stylization  $I$  is fed through the backbone DenseIBN-121 to generate the global feature map  $F \in \mathbb{R}^{D' \times W' \times H'}$ . In neural style transfer, the deep high-level semantic feature maps are utilized for driving the stylization model toward content [27], [48]. In our method,  $F$  and  $F_s$  contain high-level semantic features for input  $I$  and  $I_s$ , respectively. We hypothesize that if the model is biased toward semantic content, which is domain-irrelevant, then the predicted global feature activation map should be consistent if the model is fed with multiple copies of the same CXRs but with different style attributes. The only difference between  $I$  and  $I_s$  is the style perturbation, but the content attributes remain the same in both cases. A model that is biased towards pathological content should be robust to these variations in styles and generate a consistent global feature space. Inspired by the content loss from the literature [27], [48], we apply a content consistency regularization loss between these two global feature spaces to tweak the model's sensitivity towards content.

$$\mathcal{L}_{ccr} = \|F_s - F\|_F^2 \quad (18)$$

where,  $\|\cdot\|_F$  denotes the Frobenius norm. In addition, we also utilize the Kullback-Leibler divergence loss for regularizing the predicted probability distribution from the classifier. Let

$\mathbf{p}$  be the predicted probability distribution vector from the classifier for the CXR image without style perturbation ( $\mathbf{I}$ ). We define the probability distribution regularization loss as:

$$\mathcal{L}_{pdr} = \text{KLD}'(\mathbf{p}^s, \mathbf{p}) \quad (19)$$

Thus, the total consistency regularization loss is defined as:

$$\mathcal{L}_{cons} = \frac{\mathcal{L}_{ccr} + \mathcal{L}_{pdr}}{2} \quad (20)$$

The overall learning objective for the backbone model (without style nets) is comprised of the classification loss and consistency regularization loss and is expressed as:

$$\mathcal{L}_{total} = \mathcal{L}_{cls} + \mathcal{L}_{cons} \quad (21)$$

Note that the style randomization modules are not active during the inference stage.

#### IV. EXPERIMENTS AND RESULTS

##### A. Thoracic Disease Datasets

We utilize the three large-scale thoracic disease datasets, namely, CheXpert [23], MIMIC-CXR [24], and BRAX [25] datasets, for our experiments. The CheXpert, MIMIC-CXR, and BRAX datasets obtain 224,316 CXRs from 65,240 patients, 377,110 CXRs from 227,835 imaging studies for 65,379 patients, and 40,967 CXRs from 24,959 clinical studies, respectively. These three datasets have the same label space consisting of 14 pathologies. We follow the U-Ones policy [23] to prepare the ground truths. We use frontal CXR images and select one image per patient/study for our experiments. We use CheXpert and MIMIC-CXR datasets for training and the BRAX dataset for inference, whose distribution differs from the training datasets (as demonstrated in Fig. 1).

##### B. Training Scheme

We initialize the backbone weights with DenseIBN-121 [44] pre-trained on ImageNet [45]. We resize the CXR images to 256×256 and normalize them with the mean and standard deviation of the ImageNet training set. We randomly crop 224×224 patches during training and use a centrally cropped sub-image of 224×224 dimensions for validation and inference. We utilize horizontal flipping as the data augmentation. We use the Adam optimizer with a fixed learning rate of 0.0001 and set the batch size to 200. The parameters of the backbone model are kept frozen while training the style nets. Similarly, the parameters of the style nets are kept frozen while training the backbone model. We employ the percentage area under the receiver operating characteristic curve (AUC) for performance evaluation [7], [12]. For comparison with other methods, we utilize the multi-label stratified k-fold scheme to split the training dataset into a 5-fold cross-validation framework to report the mean and standard deviation of the evaluation metrics across the folds. We use the paired t-test between cross-validated mean AUCs for reporting statistical significance. We have implemented the entire pipeline using the PyTorch deep learning library in a hardware environment that includes an Intel Core-i9 7920X, @ 2.90 GHz CPU and 4x Nvidia GeForce RTX 2080 Ti (11 GB Memory) GPUs.

##### C. Comparison with the State-of-the-art Methods

1) *Multi-source Domain Generalization*: We conduct evaluations and compare with state-of-the-art methods on the BRAX test dataset (unseen domain) and demonstrate the domain generalization capacity of our proposed framework. We compare our proposed method with several existing state-of-the-art models, including the image-level style perturbation-based methods: STRAP [14] and AdvStyle [20]; feature-level style perturbation-based methods: FSR [22], SagNet [21], MixStyle [19], pAdaIN [29], and CrossNorm & SelfNorm [30]; and Fourier transformation based method: FDA [34]. We also compare our method with approaches developed explicitly for thoracic diseases, such as the task-specific adversarial learning approach from Luo *et al.* [7] and the multiple-domain mixup and ensemble learning approach from Wang *et al.* [12].

We have implemented the methods in the same domain generalization scenario using the same backbone model (DenseIBN-121) and common hyper-parameters, such as learning rate, image dimension, and so on. The hyper-parameters specific to the respective approaches are computed using the 5-fold cross-validation results. The results are summarized in Table I. As the results show, our proposed method achieves an average AUC of 77.18 with a standard deviation of 0.20 on the unseen domain BRAX test dataset and outperforms the state-of-the-art approaches. Our proposed method achieves the best score in 12 out of 14 pathologies while achieving competitive scores in the rest. Overall, our proposed method achieves a 1.40% absolute average AUC improvement compared to the former best method. We have also performed statistical comparisons using the paired t-test on the five-fold cross-validation scores, and the improvements are found to be significant ( $p < 0.05$ ). These results suggest that the proposed method has the ability to learn more robust, generalizable, pathology-specific, but domain-agnostic visual features compared to the existing approaches.

2) *Single-source Domain Generalization*: A more restrictive setting than that of multi-source DG is that of single-source DG, in which only one source domain is available during training. We can seamlessly extend our framework to single-source DG, as our proposed framework does not explicitly require domain labels, unlike some of the other DG methods. To demonstrate the capability of single-source DG, we train our proposed framework on only either CheXpert or MIMIC-CXR dataset, evaluate its performance on the unseen domain BRAX test dataset, and compare it with the latest DG methods. The results are reported in Table II. Here, we observe that our proposed method has achieved an average AUC of 76.69 with a standard deviation of 0.56 on the unseen domain test dataset with training only on the CheXpert dataset. With training only on the MIMIC-CXR dataset, our proposed framework has achieved a 75.08±0.76 on the unseen domain test dataset.

##### D. Analysis of Different Components

We conduct experiments to evaluate the effect of each proposed component on the unseen domain test dataset (BRAX),



TABLE I

PATHOLOGY-WISE PERFORMANCE COMPARISON OF THE PROPOSED METHOD WITH STATE-OF-THE-ART SYSTEMS ON THE BRAX DATASET<sup>†</sup> UNDER THE MULTI-SOURCE DOMAIN GENERALIZATION SETTING. THE BEST RESULT FOR EACH DISEASE CLASS IS SHOWN IN **Red**.

Method	Atel	Card	E.C.	Cons	Edem	Pne1	Pne2	P.E.	P.O.	L.L.	L.O.	Frac	S.D.	N.F.	Average	p-value <sup>‡</sup>
CrossNorm & SelfNorm [30]	74.50	86.69	65.40	67.34	75.10	86.30	78.35	85.05	83.70	58.11	70.49	61.53	77.35	70.02	74.28±0.41	0.0001*
Luo <i>et al.</i> [7]	74.81	87.12	66.70	64.42	74.89	87.47	79.51	85.80	84.40	57.45	71.50	61.49	76.83	70.33	74.48±0.78	0.0038*
FDA [34]	76.44	84.61	61.04	<b>70.01</b>	75.32	87.15	79.23	86.42	87.23	55.97	71.66	61.88	77.78	70.42	74.66±0.24	0.0001*
pAdaln [29]	75.11	86.91	65.29	67.72	74.82	87.30	77.51	86.05	87.59	59.13	71.46	62.31	77.15	70.67	74.93±0.26	0.0002*
AdvStyle [20]	74.96	86.99	66.06	68.32	75.63	87.76	78.08	86.08	88.06	58.35	71.29	62.63	76.88	70.46	75.11±0.24	<0.0001*
SagNet [21]	75.27	87.53	66.49	67.54	74.17	87.06	78.63	86.15	88.81	58.98	71.29	62.24	77.14	70.78	75.15±0.33	0.0005*
STRAP [14]	74.42	86.53	65.19	69.97	<b>76.47</b>	86.87	78.06	86.77	91.55	56.10	70.49	62.29	76.86	71.11	75.19±0.31	<0.0001*
Wang <i>et al.</i> [12]	74.96	85.90	65.75	69.48	75.50	87.68	79.45	86.49	89.65	56.99	71.16	63.67	76.91	70.27	75.28±0.29	0.0001*
MixStyle [19]	75.37	87.91	66.47	67.70	74.89	87.27	78.75	86.53	89.08	59.16	71.80	62.79	<b>77.89</b>	71.24	75.49±0.21	0.0002*
FSR [22]	75.84	87.52	68.51	69.19	76.11	87.68	78.36	85.82	87.94	58.87	72.59	63.24	77.58	71.17	75.78±0.45	0.0007*
Ours	<b>77.77</b>	<b>88.67</b>	<b>70.25</b>	68.05	74.54	<b>88.00</b>	<b>80.77</b>	<b>89.19</b>	<b>92.89</b>	<b>61.55</b>	<b>72.99</b>	<b>66.53</b>	77.10	<b>72.17</b>	<b>77.18±0.20</b>	REF

<sup>†</sup> The 14 findings are Atelectasis (Atel), Cardiomegaly (Card), Enlarged Cardiomediastinum (E.C.), Consolidation (Cons), Edema (Edem), Pneumonia (Pne1), Pneumothorax (Pne2), Pleural Effusion (P.E.), Pleural Other (P.O.), Lung Lesion (L.L.), Lung Opacity (L.O.), Fracture (Frac), Support Devices (S.D.), No Finding (N.F.).

<sup>‡</sup> A paired t-test on mean AUCs of 5-folds is used for computing statistical significance compared to the reference method (REF).

\* Indicates a significant difference.

TABLE II

PATHOLOGY-WISE PERFORMANCE COMPARISON OF THE PROPOSED METHOD WITH STATE-OF-THE-ART SYSTEMS ON THE BRAX DATASET<sup>†</sup> UNDER THE SINGLE-SOURCE DOMAIN GENERALIZATION SETTING. THE BEST RESULT FOR EACH DISEASE CLASS IS SHOWN IN **Red**.

CheXpert → BRAX																
Method	Atel	Card	E.C.	Cons	Edem	Pne1	Pne2	P.E.	P.O.	L.L.	L.O.	Frac	S.D.	N.F.	Average	p-value <sup>‡</sup>
CrossNorm & SelfNorm [30]	76.14	85.52	65.09	<b>63.23</b>	71.58	85.86	74.45	86.19	71.80	59.23	70.15	57.72	76.71	70.59	72.45±1.05	0.0007*
pAdaln [29]	76.26	85.88	69.02	61.44	71.85	84.90	78.74	87.04	81.44	60.64	70.38	59.54	76.66	70.44	73.87±0.72	0.0003*
STRAP [14]	75.65	86.50	69.73	62.60	70.91	85.70	76.88	86.91	81.15	61.11	70.00	61.10	75.85	70.64	73.91±0.90	0.0009*
SagNet [21]	75.93	86.08	68.62	61.42	71.65	85.02	78.64	86.51	82.94	60.75	70.16	60.87	76.85	70.39	73.99±0.71	<0.0001*
AdvStyle [20]	76.81	86.09	70.60	61.37	<b>73.20</b>	85.68	76.27	87.28	81.85	60.86	70.74	60.43	76.38	70.45	74.14±0.89	0.0006*
FDA [34]	77.15	86.80	70.77	61.51	71.54	83.84	77.89	87.55	80.71	61.63	70.06	61.21	76.87	70.39	74.14±0.72	0.0002*
MixStyle [19]	76.87	87.01	69.88	60.12	71.59	84.72	79.44	87.39	82.51	61.57	70.88	61.17	76.93	71.12	74.37±0.53	<0.0001*
FSR [22]	77.62	<b>88.56</b>	72.06	61.13	72.54	86.44	79.96	87.86	82.38	61.35	71.82	63.28	<b>77.36</b>	<b>72.63</b>	75.36±0.30	0.0010*
Ours	<b>78.83</b>	88.37	<b>75.73</b>	63.08	71.35	<b>86.78</b>	<b>81.45</b>	<b>89.39</b>	<b>87.66</b>	<b>63.46</b>	<b>72.24</b>	<b>65.94</b>	77.19	72.22	<b>76.69±0.56</b>	REF

MIMIC-CXR → BRAX																
Method	Atel	Card	E.C.	Cons	Edem	Pne1	Pne2	P.E.	P.O.	L.L.	L.O.	Frac	S.D.	N.F.	Average	p-value <sup>‡</sup>
CrossNorm & SelfNorm [30]	71.71	83.63	66.51	69.77	74.70	82.52	69.20	85.49	85.82	55.21	69.62	54.44	71.86	68.56	72.07±0.63	0.0029*
FDA [34]	72.98	83.61	64.28	71.00	75.12	85.67	69.71	85.70	85.41	56.27	70.53	53.99	73.45	69.89	72.69±0.29	0.0087*
SagNet [21]	72.36	85.72	68.80	70.63	73.72	83.99	70.61	85.95	84.87	<b>56.34</b>	69.67	54.79	71.41	69.85	72.77±0.62	0.0069*
pAdaln [29]	72.29	85.63	68.98	70.68	74.47	84.69	70.81	86.01	84.40	56.01	69.89	54.32	71.45	69.81	72.82±0.57	0.0066*
AdvStyle [20]	72.42	85.37	68.69	71.59	75.02	86.26	69.09	86.28	86.51	55.52	70.56	56.64	71.34	70.09	73.24±0.61	0.0064*
MixStyle [19]	72.92	85.79	68.81	70.97	74.89	85.68	71.34	86.55	85.26	55.80	70.62	55.02	71.99	70.29	73.28±0.52	0.0099*
STRAP [14]	72.12	84.09	67.26	71.63	<b>77.82</b>	86.58	69.40	85.94	88.63	54.78	70.30	55.48	73.46	69.91	73.39±0.22	0.0346*
FSR [22]	73.33	85.22	67.28	70.67	76.83	86.70	70.14	86.31	88.96	53.86	71.75	58.35	<b>74.01</b>	69.78	73.80±0.21	0.0451*
Ours	<b>74.45</b>	<b>86.34</b>	<b>69.52</b>	<b>72.09</b>	77.43	<b>87.98</b>	<b>73.80</b>	<b>87.21</b>	<b>90.68</b>	55.25	<b>72.54</b>	<b>58.95</b>	73.78	<b>71.07</b>	<b>75.08±0.76</b>	REF

<sup>†</sup> The 14 findings are Atelectasis (Atel), Cardiomegaly (Card), Enlarged Cardiomediastinum (E.C.), Consolidation (Cons), Edema (Edem), Pneumonia (Pne1), Pneumothorax (Pne2), Pleural Effusion (P.E.), Pleural Other (P.O.), Lung Lesion (L.L.), Lung Opacity (L.O.), Fracture (Frac), Support Devices (S.D.), No Finding (N.F.).

<sup>‡</sup> A paired t-test on mean AUCs of 5-folds is used for computing statistical significance compared to the reference method (REF).

\* Indicates a significant difference.

including image-level style perturbation (SRM-IL), feature-level style perturbation (SRM-FL), and consistency regularization loss ( $\mathcal{L}_{cons}$ ). The results are reported in Table III. Checkmarks in the table indicate if the specific component is incorporated. Table III shows that the image-level style perturbation (SRM-IL) and feature-level style perturbation (SRM-FL) bring 1.01% (index-ii), and 0.96% (index-iv) absolute improvement in AUC, respectively. Utilizing both modules brings 1.25% absolute AUC improvement (index-iii). Incorporating the consistency regularization loss with the image-level perturbation module adds 1.39% absolute AUC improvement (index-v). Finally, incorporating all of the proposed strategies adds another 0.46% absolute AUC improvement (index-vi), resulting in a 3.81% relative improvement compared to the baseline score.

### E. Analysis of SRM-FL

**Effect of randomization stage:** Different layers of the CNN model encode distinct visual attributes, such as lower layers

tend to encode low-level texture information while higher levels encode high-level semantic features [48], [49]. Thus, we must apply the SRM-FL at an adequate stage. This is because employing a SRM-FL to randomize too high-level feature statistics may alter the semantic content necessary for pathology prediction, while randomizing too low-level features may lead to sub-optimal performance. To evaluate the effect of the randomization stage, we apply the SRM-FL after dense block-1,2, and 3, one at a time, and measure the performances. The results are shown in part-1 of Table IV. Our experiment shows that the proposed framework performs best when the SRM-FL is applied after dense block-2.

**Sensitivity of the hyperparameter  $\eta$ :** We vary the hyperparameter  $\eta$  from 1 to 0.01 with a step of  $\frac{1}{10}$  and calculate the percentage AUC performance. The results are reported in part-2 of Table IV. From Table IV, we can observe that the SRM-FL achieves the best result when  $\eta$  equals 0.1. We speculate that  $\eta=0.1$  achieves the best score as  $\frac{\mathcal{L}_c}{\mathcal{L}_s} \approx 0.1$ . Increasing  $\eta$  too much degrades the score as it disrupts the semantic content

TABLE III

ABLATION STUDY ON THE COMPONENTS OF OUR PROPOSED METHOD. EVALUATIONS ARE CONDUCTED ON THE BRAX DATASET<sup>†</sup> AS THE UNSEEN DOMAIN TEST DATASET. THE BEST RESULT FOR EACH DISEASE CLASS IS SHOWN IN **RED**.

Indices	Baseline	SRM-IL	SRM-FL	$\mathcal{L}_{cons}$	Atel	Card	E.C.	Cons	Edem	Pne1	Pne2	P.E.	P.O.	L.L.	L.O.	Frac	S.D.	N.F.	Average
(i)	✓				74.89	86.79	68.98	69.72	75.05	87.97	78.11	86.77	87.88	58.18	71.16	57.78	77.19	70.12	75.04
(ii)	✓	✓			76.78	86.88	67.20	69.20	<b>77.81</b>	<b>88.89</b>	79.82	87.82	90.04	58.56	72.41	60.98	77.35	71.00	76.05
(iii)	✓	✓	✓		76.11	86.93	65.30	<b>72.15</b>	74.74	87.62	<b>83.30</b>	86.15	90.13	59.57	72.65	64.24	<b>78.08</b>	71.07	76.29
(iv)	✓		✓		74.62	87.38	68.40	69.34	77.43	88.16	82.57	87.22	90.48	57.93	70.88	62.90	76.47	70.21	76.00
(v)	✓	✓		✓	77.68	88.51	69.17	69.51	77.38	88.23	81.88	89.62	92.47	59.63	73.28	66.77	77.83	72.27	77.44
(vi)	✓	✓	✓	✓	<b>78.12</b>	<b>89.93</b>	<b>71.22</b>	69.45	76.72	87.79	81.46	<b>89.63</b>	<b>93.74</b>	<b>60.78</b>	<b>73.36</b>	<b>68.33</b>	77.40	<b>72.73</b>	<b>77.90</b>

<sup>†</sup> The 14 findings are Atelectasis (Atel), Cardiomegaly (Card), Enlarged Cardiomediastinum (E.C.), Consolidation (Cons), Edema (Edem), Pneumonia (Pne1), Pneumothorax (Pne2), Pleural Effusion (P. E.), Pleural Other (P.O.), Lung Lesion (L.L.), Lung Opacity (L.O.), Fracture (Frac), Support Devices (S.D.), No Finding (N.F.).

TABLE IV

ANALYSIS OF THE FEATURE-LEVEL STYLE RANDOMIZATION MODULE ON THE BRAX DATASET<sup>†</sup> AS THE UNSEEN DOMAIN. THE BEST RESULT FOR EACH DISEASE CLASS IS SHOWN IN **RED**.

Method	Atel	Card	E.C.	Cons	Edem	Pne1	Pne2	P.E.	P.O.	L.L.	L.O.	Frac	S.D.	N.F.	Average
<b>Part-1: Investigation of the effect of randomization stage</b>															
DB-1	77.68	88.51	69.17	<b>69.51</b>	<b>77.38</b>	88.23	<b>81.88</b>	89.62	92.47	59.63	73.28	66.77	<b>77.83</b>	72.27	77.44
DB-2	78.12	<b>89.93</b>	<b>71.22</b>	69.45	76.72	87.79	81.46	<b>89.63</b>	<b>93.74</b>	60.78	<b>73.36</b>	<b>68.33</b>	77.40	<b>72.73</b>	<b>77.90</b>
DB-3	<b>78.16</b>	89.17	68.22	67.42	74.66	<b>88.54</b>	77.16	89.14	92.44	<b>61.11</b>	73.20	66.20	75.77	72.25	76.67
<b>Part-2: Investigation of the effect of hyper-parameter <math>\eta</math></b>															
$\eta=1$	77.96	89.40	68.87	66.26	75.66	86.91	81.70	89.43	92.32	60.11	<b>73.46</b>	<b>68.55</b>	76.80	72.46	77.13
$\eta=0.1$	<b>78.12</b>	<b>89.93</b>	<b>71.22</b>	69.45	<b>76.72</b>	87.79	81.46	89.63	<b>93.74</b>	<b>60.78</b>	73.36	68.33	<b>77.40</b>	<b>72.73</b>	<b>77.90</b>
$\eta=0.01$	77.99	88.67	69.70	68.64	75.75	<b>88.00</b>	<b>82.04</b>	<b>89.80</b>	93.42	59.90	73.40	67.28	76.84	72.38	77.42
<b>Part-3: Effect of learnable style embeddings</b>															
Pre-defined	78.03	89.12	69.12	69.12	76.02	<b>88.19</b>	78.00	<b>89.79</b>	91.57	<b>60.93</b>	<b>73.81</b>	<b>69.02</b>	76.15	72.62	77.25
Learnable	<b>78.12</b>	<b>89.93</b>	<b>71.22</b>	69.45	<b>76.72</b>	87.79	<b>81.46</b>	89.63	<b>93.74</b>	60.78	73.36	68.33	<b>77.40</b>	<b>72.73</b>	<b>77.90</b>
<b>Part-4: Analysis of the style net architecture</b>															
Conv	78.12	<b>89.93</b>	<b>71.22</b>	69.45	76.72	87.79	81.46	89.63	93.74	<b>60.78</b>	73.36	68.33	<b>77.40</b>	<b>72.73</b>	<b>77.90</b>
Conv+ReLU	77.17	88.58	69.30	67.74	<b>77.02</b>	87.37	<b>82.54</b>	89.34	92.77	59.22	72.89	<b>69.29</b>	75.85	72.07	77.23
Conv+BN	<b>78.40</b>	89.09	67.65	69.17	74.37	87.30	80.25	<b>89.95</b>	<b>93.86</b>	60.68	<b>73.70</b>	68.91	77.00	72.67	77.38

<sup>†</sup> The 14 findings are Atelectasis (Atel), Cardiomegaly (Card), Enlarged Cardiomediastinum (E.C.), Consolidation (Cons), Edema (Edem), Pneumonia (Pne1), Pneumothorax (Pne2), Pleural Effusion (P. E.), Pleural Other (P.O.), Lung Lesion (L.L.), Lung Opacity (L.O.), Fracture (Frac), Support Devices (S.D.), No Finding (N.F.).

features. Decreasing the  $\eta$  too much reduces the style diversity of the SRM-FL, resulting in performance loss.

**Impact of learnable style embeddings:** To evaluate the impact of the learnable pixel-wise affine parameters as the style embeddings compared to the pre-defined style embeddings, we replace the style nets in the SRM-FL with the AdaIN module [27] and compute the percentage AUC score. The results are reported in part-3 of Table IV. We can observe that the learnable pixel-wise affine parameters achieve better results compared to pre-defined style embedding parameters.

**Analysis of the style net architecture:** The style nets  $\phi_\gamma$  and  $\phi_\beta$  contain only convolutional (Conv) layers. We conduct experiments adding a rectified linear layer (ReLU) and a batch normalization (BN) layer after the convolutional layers, respectively. The results are reported in Table IV. We can observe that the style nets with only convolutional layers achieve the best score. We speculate that the style parameters are set as the affine parameters, and as the affine parameters do not necessarily lie on the positive plane, the utilization of ReLU results in lower performance because it limits the learnable parameter range. In the case of BN, we speculate that the population statistics may interfere with instance statistics, as each single pair (content and style reference sample) has different styles.

## V. CONCLUSION

In this paper, we propose a DG framework that extracts domain-invariant features by making a deep learning model style invariant and biased toward content. To the best of our knowledge, no previous DG study for thoracic disease detection has exploited neural style transfer to develop a domain-agnostic model. We deploy SRMs both at the image and feature level to augment the style characteristics and employ consistency regularizations to tweak the backbone model's sensitivity towards semantic content rather than uninformative texture, i.e., styles, for pathology prediction. Extensive experiments with three large-scale thoracic disease datasets demonstrate significantly improved performance and generalizability compared to the baseline and state-of-the-art methods on the unseen domain test dataset.

## REFERENCES

- [1] X. Ouyang *et al.*, "Learning hierarchical attention for weakly-supervised chest X-ray abnormality localization and diagnosis," *IEEE Trans. Med. Imaging*, vol. 40, no. 10, pp. 2698–2710, 2021.
- [2] Y. Zhou, T. Zhou, T. Zhou, H. Fu, J. Liu, and L. Shao, "Contrast-attentive thoracic disease recognition with dual-weighting graph reasoning," *IEEE Trans. Med. Imaging*, vol. 40, no. 4, pp. 1196–1206, 2021.
- [3] U. Kamal, M. Zunaed, N. B. Nizam, and T. Hasan, "Anatomy-XNet: An anatomy aware convolutional neural network for thoracic disease classification in chest X-rays," *IEEE J. Biomed. Health Inform.*, vol. 26, no. 11, pp. 5518–5528, 2022.
- [4] Z. Lin *et al.*, "AANet: Adaptive attention network for covid-19 detection from chest X-ray images," *IEEE Trans. Neural Netw. Learn. Syst.*, vol. 32, no. 11, pp. 4781–4792, 2021.



- [5] P. Bhowal, S. Sen, J. H. Yoon, Z. W. Geem, and R. Sarkar, "Choquet integral and coalition game-based ensemble of deep learning models for covid-19 screening from chest X-ray images," *IEEE J. Biomed. Health Inform.*, vol. 25, no. 12, pp. 4328–4339, 2021.
- [6] J. Quiñero-Candela, M. Sugiyama, A. Schwaighofer, and N. D. Lawrence, *Dataset Shift in Machine Learning*. MIT Press, 2009.
- [7] L. Luo *et al.*, "Deep mining external imperfect data for chest X-ray disease screening," *IEEE Trans. Med. Imaging*, vol. 39, no. 11, pp. 3583–3594, 2020.
- [8] R. Zhang, F. Yang, Y. Luo, J. Liu, and C. Wang, "Learning invariant representation for unsupervised domain adaptive thorax disease classification," *Pattern Recognit. Lett.*, vol. 160, pp. 155–162, 2022.
- [9] Y. Feng *et al.*, "Deep supervised domain adaptation for pneumonia diagnosis from chest X-ray images," *IEEE J. Biomed. Health Inform.*, vol. 26, no. 3, pp. 1080–1090, 2022.
- [10] C. He, L. Zheng, T. Tan, X. Fan, and Z. Ye, "Multi-attention representation network partial domain adaptation for covid-19 diagnosis," *Appl. Soft Comput.*, vol. 125, p. 109205, 2022.
- [11] J. Zhou, B. Jing, Z. Wang, H. Xin, and H. Tong, "SODA: Detecting covid-19 in chest X-rays with semi-supervised open set domain adaptation," *IEEE/ACM Trans. Comput. Biol. Bioinform.*, vol. 19, no. 5, pp. 2605–2612, 2022.
- [12] H. Wang and Y. Xia, "Domain-ensemble learning with cross-domain mixup for thoracic disease classification in unseen domains," *Biomed. Signal Process. Control*, vol. 81, p. 104488, 2023.
- [13] L. Zhang *et al.*, "Generalizing deep learning for medical image segmentation to unseen domains via deep stacked transformation," *IEEE Trans. Med. Imaging*, vol. 39, no. 7, pp. 2531–2540, 2020.
- [14] R. Yamashita, J. Long, S. Banda, J. Shen, and D. L. Rubin, "Learning domain-agnostic visual representation for computational pathology using medically-irrelevant style transfer augmentation," *IEEE Trans. Med. Imaging*, vol. 40, no. 12, pp. 3945–3954, 2021.
- [15] C. Li *et al.*, "Domain generalization on medical imaging classification using episodic training with task augmentation," *Comput. Biol. Med.*, vol. 141, p. 105144, 2022.
- [16] N. Baker, H. Lu, G. Erlikhman, and P. J. Kellman, "Deep convolutional networks do not classify based on global object shape," *PLoS Comput. Biol.*, vol. 14, no. 12, pp. 1–43, 12 2018.
- [17] R. Geirhos, P. Rubisch, C. Michaelis, M. Bethge, F. A. Wichmann, and W. Brendel, "Imagenet-trained CNNs are biased towards texture; increasing shape bias improves accuracy and robustness," in *ICLR*, 2019.
- [18] P. T. Jackson, A. Atapour-Abarghouei, S. Bonner, T. P. Breckon, and B. Obara, "Style Augmentation: Data augmentation via style randomization," in *IEEE CVPR Workshops*, 2019, pp. 83–92.
- [19] K. Zhou, Y. Yang, Y. Qiao, and T. Xiang, "Domain generalization with mixstyle," *ICLR*, 2021.
- [20] Z. Zhong, Y. Zhao, G. H. Lee, and N. Sebe, "Adversarial style augmentation for domain generalized urban-scene segmentation," *Adv. neural inf. process. syst.*, vol. 35, pp. 338–350, 2022.
- [21] H. Nam, H. Lee, J. Park, W. Yoon, and D. Yoo, "Reducing domain gap by reducing style bias," in *IEEE CVPR*, 2021, pp. 8686–8695.
- [22] Y. Wang, L. Qi, Y. Shi, and Y. Gao, "Feature-based style randomization for domain generalization," *IEEE Trans. Circuits Syst. Video Technol.*, vol. 32, no. 8, pp. 5495–5509, 2022.
- [23] J. Irvin *et al.*, "Chexpert: A large chest radiograph dataset with uncertainty labels and expert comparison," *AAAI*, vol. 33, pp. 590–597, 7 2019.
- [24] A. E. W. Johnson *et al.*, "Mimic-cxr, a de-identified publicly available database of chest radiographs with free-text reports," *Sci. Data*, vol. 6, p. 317, 2019.
- [25] E. P. Reis *et al.*, "Brax, Brazilian labeled chest X-ray dataset," *Sci. Data*, vol. 9, p. 487, 2022.
- [26] L. van der Maaten and G. Hinton, "Visualizing data using t-sne," *J. Mach. Learn. Res.*, vol. 9, no. 86, pp. 2579–2605, 2008.
- [27] X. Huang and S. Belongie, "Arbitrary style transfer in real-time with adaptive instance normalization," in *IEEE ICCV*, 2017, pp. 1510–1519.
- [28] G. Huang, Z. Liu, L. Van Der Maaten, and K. Q. Weinberger, "Densely connected convolutional networks," in *IEEE CVPR*, 2017, pp. 2261–2269.
- [29] O. Nuriel, S. Benaim, and L. Wolf, "Permuted AdaIN: Reducing the bias towards global statistics in image classification," in *IEEE CVPR*, 2021, pp. 9477–9486.
- [30] Z. Tang, Y. Gao, Y. Zhu, Z. Zhang, M. Li, and D. Metaxas, "CrossNorm and SelfNorm for generalization under distribution shifts," in *IEEE ICCV*, 2021, pp. 52–61.
- [31] H. Guan and M. Liu, "Domain adaptation for medical image analysis: A survey," *IEEE Trans. Biomed. Eng.*, vol. 69, no. 3, pp. 1173–1185, 2022.
- [32] D. D. Pham, S. M. Koesnadi, G. Dovletov, and J. Pauli, "Unsupervised adversarial domain adaptation for multi-label classification of chest X-ray," in *IEEE ISBI*, 2021, pp. 1236–1240.
- [33] X. Chen *et al.*, "Dual adversarial attention mechanism for unsupervised domain adaptive medical image segmentation," *IEEE Trans. Med. Imaging*, vol. 41, no. 11, pp. 3445–3453, 2022.
- [34] Y. Yang and S. Soatto, "FDA: Fourier domain adaptation for semantic segmentation," in *IEEE CVPR*, 2020, pp. 4084–4094.
- [35] K. Sanchez, C. Hinojosa, H. Arguello, D. Kouamé, O. Meyrignac, and A. Basarab, "CX-DaGAN: Domain adaptation for pneumonia diagnosis on a small chest X-ray dataset," *IEEE Trans. Med. Imaging*, vol. 41, no. 11, pp. 3278–3288, 2022.
- [36] M. T. Shaban, C. Baur, N. Navab, and S. Albarqouni, "Staingan: Stain style transfer for digital histological images," in *IEEE ISBI*, 2019, pp. 953–956.
- [37] P. Diao, A. Pai, C. Igel, and C. H. Krag, "Histogram-based unsupervised domain adaptation for medical image classification," *MICCAI*, pp. 755–764, 2022.
- [38] Y. Ganin *et al.*, "Domain-adversarial training of neural networks," *J. Mach. Learn. Res.*, vol. 17, no. 1, p. 2096–2030, jan 2016.
- [39] Y. Du *et al.*, "Learning to learn with variational information bottleneck for domain generalization," *ECCV*, pp. 200–216, 2020.
- [40] M. Segu, A. Tonioni, and F. Tombari, "Batch normalization embeddings for deep domain generalization," *Pattern Recognit*, vol. 135, p. 109115, 2023.
- [41] D. Ulyanov, A. Vedaldi, and V. Lempitsky, "Improved texture networks: Maximizing quality and diversity in feed-forward stylization and texture synthesis," in *IEEE CVPR*, 2017, pp. 4105–4113.
- [42] T. Miyato, S.-I. Maeda, M. Koyama, and S. Ishii, "Virtual adversarial training: A regularization method for supervised and semi-supervised learning," *IEEE Trans. Pattern Anal. Mach. Intell.*, vol. 41, no. 8, pp. 1979–1993, 2019.
- [43] J. Hu, L. Shen, and G. Sun, "Squeeze-and-Excitation networks," in *IEEE CVPR*, 2018, pp. 7132–7141.
- [44] X. Pan, P. Luo, J. Shi, and X. Tang, "Two at once: Enhancing learning and generalization capacities via IBN-Net," in *Eur. Conf. Comput. Vis.*, 2018, pp. 484–500.
- [45] J. Deng, W. Dong, R. Socher, L.-J. Li, K. Li, and L. Fei-Fei, "ImageNet: A large-scale hierarchical image database," in *IEEE CVPR*, 2009, pp. 248–255.
- [46] Y. Han *et al.*, "Knowledge-augmented contrastive learning for abnormality classification and localization in chest X-rays with radiomics using a feedback loop," in *IEEE WACV*, 2022, pp. 2465–2474.
- [47] T.-Y. Lin, P. Goyal, R. Girshick, K. He, and P. Dollár, "Focal loss for dense object detection," in *IEEE ICCV*, 2017, pp. 2999–3007.
- [48] L. Gatys, A. S. Ecker, and M. Bethge, "Texture synthesis using convolutional neural networks," in *Adv. neural inf. process. syst.*, vol. 28, 2015.
- [49] T. Karras, S. Laine, and T. Aila, "A style-based generator architecture for generative adversarial networks," *IEEE Trans. Pattern Anal. Mach. Intell.*, vol. 43, no. 12, pp. 4217–4228, dec 2021.